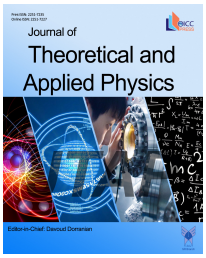

Volume 19, Issue 5, 192549 (1-15)

Journal of Theoretical and Applied Physics (JTAP)

https://doi.org/10.57647/j.jtap.2025.1905.49

Turbulent boundary layer/shock wave interaction in a nozzle using a compressible lattice Boltzmann method

Hiwa Hosseini, Ebrahim Goshtasbi Rad*

Department of Mechanical Engineering, Shiraz University, Shiraz, Iran.

***Corresponding author:** goshtasb@shirazu.ac.ir

Original Research

Received:
23 May 2025
Revised:
29 August 2025
Accepted:
4 September 2025
Published online:
30 September 2025

Abstract:

The double distribution function lattice Boltzmann method (DDF-LBM) is explored for its potential use in a single expansion ramp nozzle. The main goal is to evaluate how well DDF-LBM can model shock wave/boundary layer interactions (SWBLI), including shock formation and the size of separation bubbles. The method which is validated in a previous paper by the same authors by examining its potential strengths in well-known benchmark problems such as the shock tube and flow around an airfoil, is combined with Spallart-Almaras turbulent model to simulate shock wave and turbulent boundary layer interactions near a nozzle wall. Achieving accurate results required careful attention to spatial discretization, selecting suitable Courant-Friedrichs-Lewy (CFL) numbers, and tuning parameters. The effectiveness of two discretization schemes—the fifth-order weighted essentially non-oscillatory (WENO) and the third-order weighted non-free-parameter dissipation (WNND)-was assessed for capturing key physical phenomena. The influence of the entrance Mach number was also studied to evaluate the method's ability to predict major flow variations.

Keywords: Lattice Boltzmann method; Compressible flow; Shock wave/boundary layer interaction

1. Introduction

Over the last thirty years, the lattice Boltzmann method (LBM) has garnered significant interest among researchers and academics. Its popularity stems from its straightforwardness, compatibility with parallel computing, and capacity to handle complex geometries. Rooted in the fundamental Boltzmann equation, well-known techniques like the Chapman-Enskog expansion link the microscopic dynamics in LBM to macroscopic conservation laws. Acting as an intermediary between micro- and macro-scales, the recent form of LBM operates at the mesoscopic level, effectively capturing key aspects of fluid flow. Though its origins lie in lattice gas automata, its current iteration results from discretizing the Boltzmann equation in velocity space, along with space and time. Since the Boltzmann equation incorporates all the necessary physics, LBM is used across a broad spectrum of computational fluid dynamics applications.

A thorough review by Dolling in 2001 [1] examined research on shock wave-boundary layer interaction spanning the previous 50 years. Despite notable progress in numerical techniques and experimental research, several challenges still exist. Problems such as exaggerated temperature increases and unsteady pressure loads continue to be areas of concern. Although the author is optimistic about future advancements, constraints like time, cost, and the complexity of aerial missions highlight the need for a detailed understanding of the underlying physics and highly accurate simulation outcomes.

In a 2008 PhD thesis, Kun [2] proposed a new lattice Boltzmann (LB) model along with corresponding equilibrium distribution functions tailored for simulating compressible flows. Instead of using the complex Maxwell equations, the study simplifies the process by introducing an equilibrium function that satisfies the necessary conditions to recover the Navier-Stokes (NS) equations. This function is distributed across lattice sites in velocity space through Lagrangian interpolation. Using this framework, several models were developed for both compressible and incompressible, as well as viscous and inviscid flows. The discrete Boltzmann equation was solved via the finite volume method, which effectively captures shock waves and other discontinuities at high Mach numbers. The study also considers various boundary conditions, such as slip and no-slip walls. The validity of these models and the solution approach was confirmed through comparisons with existing literature, and numerical results showed that the method can successfully

simulate flows at Mach numbers as high as 10.

In 2012, Xu et al. [3] reviewed their group's work on compressible lattice Boltzmann methods. They categorized their research into three main areas: single relaxation time LBM with an added viscosity term, multiple relaxation time models, and studies of hydrodynamic instabilities. These instabilities, which occur in many natural and industrial processes, are primarily classified into Rayleigh-Taylor (RT), Richtmyer-Meshkov (RM), and Kelvin-Helmholtz (KH) types.

Then, in 2014, Li and Zhang [4] investigated compressible flows using the lattice Boltzmann method. Their approach, based on a multispeed lattice, introduced an extra distribution function to incorporate potential energy and enable the recovery of Navier-Stokes equations. They used Chapman-Enskog expansion to derive the equilibrium density distribution function in 2D with 17 discrete velocities. Equations were discretized with a third-order upwind scheme, and a von Albada limiter was applied to suppress unwanted numerical oscillations. Validation was carried out through simulations of the Riemann problem, Couette flow, and a NACA0012 airfoil, with detailed initial conditions and parameters.

In 2007, Li et al. [5] introduced a well-known double distribution function (DDF) model that uses a circular function to derive the equilibrium distribution. They selected this DDF approach to simulate shock and boundary layer interactions at the entrance of a diffuser in supersonic flows. After initial validation against the standard shock tube problem, the model was applied to two-dimensional scenarios to assess its ability to handle compressible viscous flows, particularly those involving shock waves and boundary layers with complex features.

Then, in 2017, Qiu et al. [6] employed the DDF-based LB model developed by Li et al. [5] to simulate various compressible viscous flows. They successfully validated their approach by solving the Riemann problem and Couette flow. Following this, they modeled three specific cases: A compressible boundary layer, a shock wave, and shock wave/boundary layer interaction. They also examined laminar supersonic flow over an insulated flat plate at Mach numbers 2, 4, and 6 to analyze the numerical results across different flow regimes.

Jammalamadka et al. [7] studied the classic shock wave-boundary layer interaction (SWBLI) using an LBM-based Large Eddy Simulation (VLES). Their 3D unsteady simulations focused on Mach 1.7, performed with the commercial PowerFLOW software, which employed variable refinement regions to improve grid resolution. Turbulence was initiated using a zig-zag strip. They observed an anti-correlation between temperature and velocity fields-when one increased, the other decreased. Vortical structures were visualized in 3D, and results from 2D and 3D simulations showed strong agreement. The study also captured low-frequency oscillations in the shock system, highlighting complex unsteady behavior.

In another study, Qiu et al. [8] examined non-equilibrium effects in a shock tube using a mesoscopic kinetic approach that detailed molecular velocity distributions. They analyzed the hydrodynamic and thermodynamic impacts of shock waves, contact discontinuities, and rarefaction waves. Their findings indicated that non-equilibrium effects are more significant in shock waves than in contact discontinuities or rarefaction waves. Although these effects are strong in shock waves, they are inherently unstable-the interaction with contact discontinuities alters their direction, and interactions with rarefaction waves produce sharp peaks or crests in the non-equilibrium kinetic moments, revealing complex physical behaviors.

Another application of a double distribution function lattice Boltzmann method is proposed by Bhadauria et al. [9] where the fluid-solid interaction is investigated for a compressible flow. A body-fitted spatial discretization scheme is exploited in a Lagrangian-Eulerian framework along with polynomial functions to account for local deformation of the mesh domain. Problems such as vorticity-induced vibrations on cylinders are studied to analyze dynamic behavior.

This study aims to assess the capability of a double-distribution-function-based lattice Boltzmann method (DDF-LBM) in accurately capturing the complex physics of shock wave turbulent boundary layer interactions (SWBLI). Validation results are presented in a previous paper by authors in Hosseini & Goshtasbi Rad [10]. The method is applied to a 2D nozzle flow scenario to evaluate its effectiveness in predicting shock-boundary layer interactions near nozzle walls. Additionally, the study explores the impact of different discretization schemes and varying entrance Mach numbers on simulation accuracy and robustness.

2. Methodology

Double distribution function methods evolved upon the fact that energy needs a separate distribution function to be coupled with the density distribution function via the equation of state and acts as a serious alternative for conventional CFD methods in solving Navier-Stokes equations. Accordingly, there will be another equilibrium distribution function for energy. The method by Li et al. [5] along with corresponding WENO and WNND discretization schemes are outlined in Hosseini & GoshtasbiRad [10] and we do not repeat the equations here for limitation purposes.

In order to correct the viscosity in turbulent flows, the well-known one-equation Spalart-Allmaras (SA) model was exploited which gives satisfying results in near-wall and boundary layer flows which have adverse pressure gradient. The original SA model calculates viscosity according to the following equation:

$$\frac{D\tilde{\nu}}{Dt} = C_{b_1}(1-f_{t_2})\tilde{S}\tilde{\nu} + \frac{1}{\sigma}\left[\nabla\cdot\left((\nu_l+\tilde{\nu})\nabla\tilde{\nu}\right) + C_{b_2}|\nabla\tilde{\nu}|^2\right] - (C_{w_1}f_w - \frac{C_{b_1}}{\kappa^2}f_{t_2})(\frac{\tilde{\nu}}{d})^2 \tag{1}$$

In which ν_l is the laminar flow kinematic viscosity. The eddy viscosity ν_t is defined as:

$$\nu_t = \tilde{\nu}f_{v_1},\ \ f_{v_1} = \frac{\chi^3}{\chi^3+C_{v_v}^3},\ \ \chi = \frac{\tilde{\nu}}{\nu_t} \tag{2}$$

Then, the dynamic viscosity of the turbulent flow is calculated according to $\mu_t = \rho \nu_t$. Parameters in the equations above are summarized in the following.

$$
\begin{aligned}
f_{t_2} &= C_{t_3} \exp(-C_{t_4}\chi^2) \\
\tilde{S} &= \sqrt{2\Omega_{ij}\Omega_{ij}} f_{v_3} + \frac{\tilde{\nu}}{\kappa^2 d^2} f_{v_2} \\
\Omega_{ij} &= \frac{1}{2}\left(\frac{\partial u_i}{\partial x_j} - \frac{\partial u_j}{\partial x_i}\right) \\
f_{v_2} &= 1 - \frac{\chi}{1+\chi f_{v_1}} \\
f_{v_3} &= 1 \\
f_w &= g\left(\frac{1+C_{w_3}^6}{g^6 + C_{w_3}^6}\right)^{\frac{1}{6}} \\
g &= r + C_{w_2}(r^6 - r) \\
r &= \frac{\tilde{\nu}}{S\kappa^2 d^2}
\end{aligned}
\tag{3}
$$

Constants are defined as:

$$
\begin{aligned}
&C_{b_1} = 0.1355, \quad C_{b_2} = 0.622, \quad \sigma = 2/3, \\
&\kappa = 0.41, \quad C_{w_1} = \frac{C_{b_1}}{\kappa^2} + \frac{1+C_{b_1}}{\sigma}, \quad C_{w_2} = 0.3, \\
&C_{w_3} = 2, \quad C_{v_1} = 7.1, \quad C_{t_3} = 1.1, \\
&C_{t_4} = 2
\end{aligned}
\tag{4}
$$

An improvement is suggested for better convergence which is:

$$
\begin{aligned}
&\tilde{S} = \sqrt{2\Omega_{ij}\Omega_{ij}} f_{v_3} + \frac{\tilde{\nu}}{\kappa^2 d^2} f_{v_2}, \qquad f_{v_2} = (1 + \frac{\chi}{C_{v_2}})^{-3} \\
&f_{v_3} = \frac{(1+\chi f_{v_1})(1-f_{v_2})}{\chi}, \qquad \chi = \max\{\chi \cdot 10^{-4}\}
\end{aligned}
\tag{5}
$$

To adopt the model to compressible flows, equation (1) is rewritten as follows:

$$
\begin{aligned}
\frac{\partial \tilde{\nu}}{\partial t} + \frac{\partial}{\partial x_j}(\tilde{\nu} u_j) &= \frac{D\tilde{\nu}}{Dt} + \tilde{\nu}\nabla \cdot \mathbf{u} \\
&= C_{b_1}(1 - f_{t_2})\tilde{S}\tilde{\nu} \\
&+ \frac{1}{\sigma}\left[\nabla \cdot \left((\nu_l + \tilde{\nu})\nabla\tilde{\nu}\right) + C_{b_2}|\nabla\tilde{\nu}|^2\right] \\
&- (C_{w_1} f_w - \frac{C_{b_1}}{\kappa^2} f_{t_2})(\frac{\tilde{\nu}}{d})^2
\end{aligned}
\tag{6}
$$

Finally, the improved *SA* model is expressed as:

$$
\begin{aligned}
\frac{D\tilde{\nu}}{Dt} &= [C_{b_1}(1 - f_{t_2})\tilde{S} - \nabla \cdot \mathbf{u}]\tilde{\nu} \\
&+ \frac{1}{\sigma}\left[\nabla \cdot \left((\nu_l + \tilde{\nu})\nabla\tilde{\nu}\right) + C_{b_2}|\nabla\tilde{\nu}|^2\right] \\
&- [(C_{w_1} f_w - \frac{C_{b_1}}{\kappa^2} f_{t_2})](\frac{\tilde{\nu}}{d})^2
\end{aligned}
\tag{7}
$$

And variables related to dynamic viscosity are:

$$
\mu = \mu_l + \mu_t, \quad \frac{\mu}{Pr} = \frac{\mu_l}{Pr_l} + \frac{\mu_t}{Pr_t} \tag{8}
$$

In which subscripts l and t are used for laminar and turbulent flows respectively and Pr is the Prandtl number. According to the modifications above, the relaxation times for density and total energy will be as follows:

$$
\tau_f = \frac{\mu_l + \mu_t}{p}, \quad \tau_h = \frac{1}{p}(\frac{\mu_l}{Pr_l} + \frac{\mu_t}{Pr_t}) \tag{9}
$$

3. Results and discussion

As the main concentration of this study, a typical 2D geometry of a nozzle is constructed to be studied by the DDF LBM. The corresponding geometry is illustrated in figure 1. It consists of a straight expansion ramp with a ramp angle of 25° and an expansion area ratio of 2.896. A uniform rectangular grid is used in this study and other settings for the simulation are as: $\gamma = 1.4$, $Pr = 0.71$, $R = 1$, $\mu = 1/Re$.

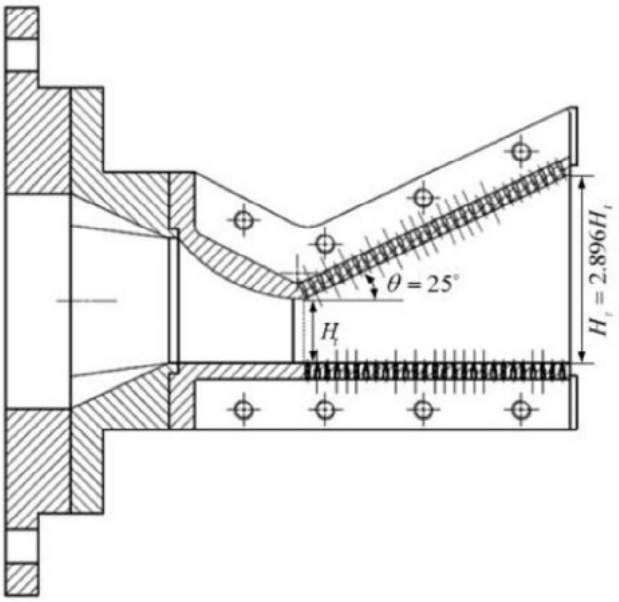

Figure 1. Geometry of the nozzle.

A C++ program was developed to carry out the computations. Different parts of the problem from the equilibrium to the discretization schemes are all written in separate functions to be called in their appropriate sequence.

Two different grid sizes were selected to be tested in the simulations, namely, a 200 × 200 and a 300 × 300 grid using the WENO discretization scheme.

Since there is no considerable discrepancy between two grids (figure 2), the smaller one with 40000 elements was chosen. An internal flow is considered for this study with the right boundary as outflow and the upper one as an open boundary condition while the surface wall (bottom boundary) is set to be bounce-back type for which a special function is provided in the flux calculation step. In this function, wall nodes are firstly identified by calling another function and then the no slip bounce back method is applied. Regarding the computational domain, it should be mentioned that a chord length of 1 is considered in our computational code to care for length units, and the computational domain is three chord lengths for both horizontal and vertical directions. Also, the grid is uniform with equal spatial increments in both directions. Three ghost layers are considered at each boundary. For the WENO scheme, solutions diverge for

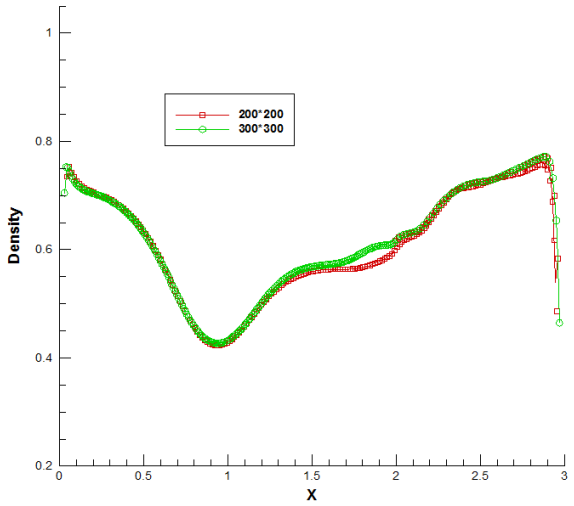

Figure 2. Density distribution on the wall for two different mesh sizes (40000 and 90000 elements).

CFL numbers more than 0.5 while for the WNND scheme gives acceptable results at CFL numbers smaller than 0.7 so a CFL number of 0.5 is selected to get acceptable results by both discretization schemes. For a flow entering the nozzle at M = 0.5, inlet temperature and pressure of 300 K and 93243.6648 Pa, respectively and exit temperature and pressure of 300 K and 31073.02 Pa, respectively; contours of density gradients are extracted for both WENO and WNND schemes and results are compared to other references.

Figures 3 and 4 show the distributions of density gradient for a single ramp expansion nozzle using WENO and WNND schemes, respectively. Results of the WENO scheme are closer to the results of Mousavi et al. [11] with respect to the lambda shock location and magnitude.

For the case of turbulent flow, two values of entrance Mach numbers namely 0.5 and 0.8 (with corresponding Reynolds

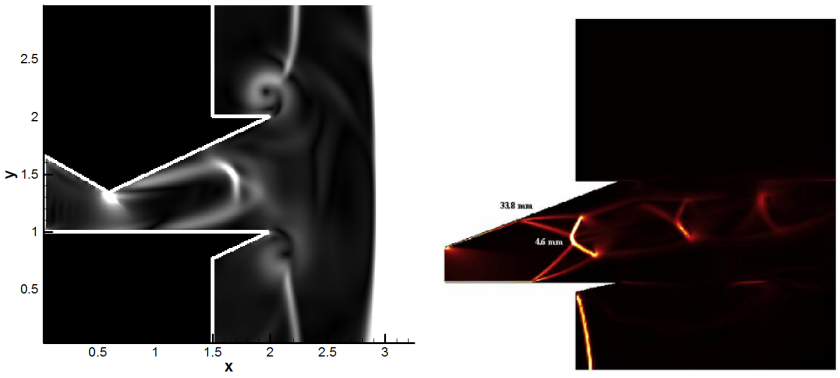

(a) **(b)**

Figure 3. Density gradient (a: WENO, b: Mousavi et al. [11])

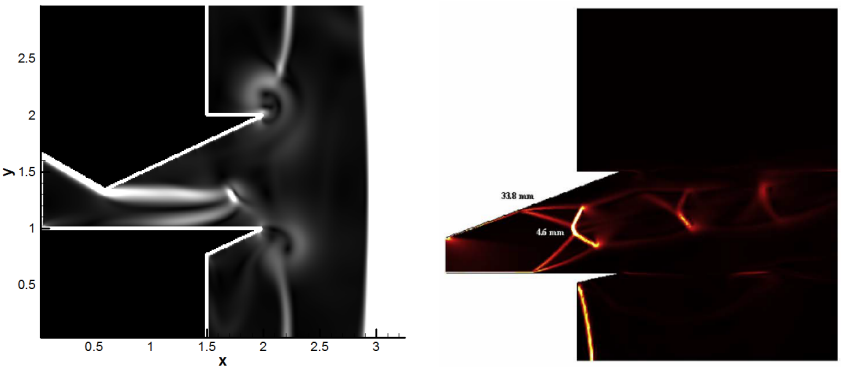

(a) **(b)**

Figure 4. Density gradient (a: WNND, b: Mousavi et al. [11]).

numbers of 650000 and 1040000 respectively) are considered to compare the applicability of WENO and WNND discretization schemes. Density gradients are plotted in the following figures.

Based on figures 5 and 6, at 0.5 seconds, the flow has not yet experienced significant growth, and flow patterns are beginning to appear near the nozzle inlet, indicating the initial formation of vortices or early instabilities in the flow. By 1.5 seconds, multiple instabilities and vortices are observed in the flow, especially in the midsection of the nozzle, signifying the development and spreading of waves and vortex structures. At 2 and 2.5 seconds, these vortices and flow structures become more evident and complex.

Figures 7 and 8, presented below, illustrate the evolution

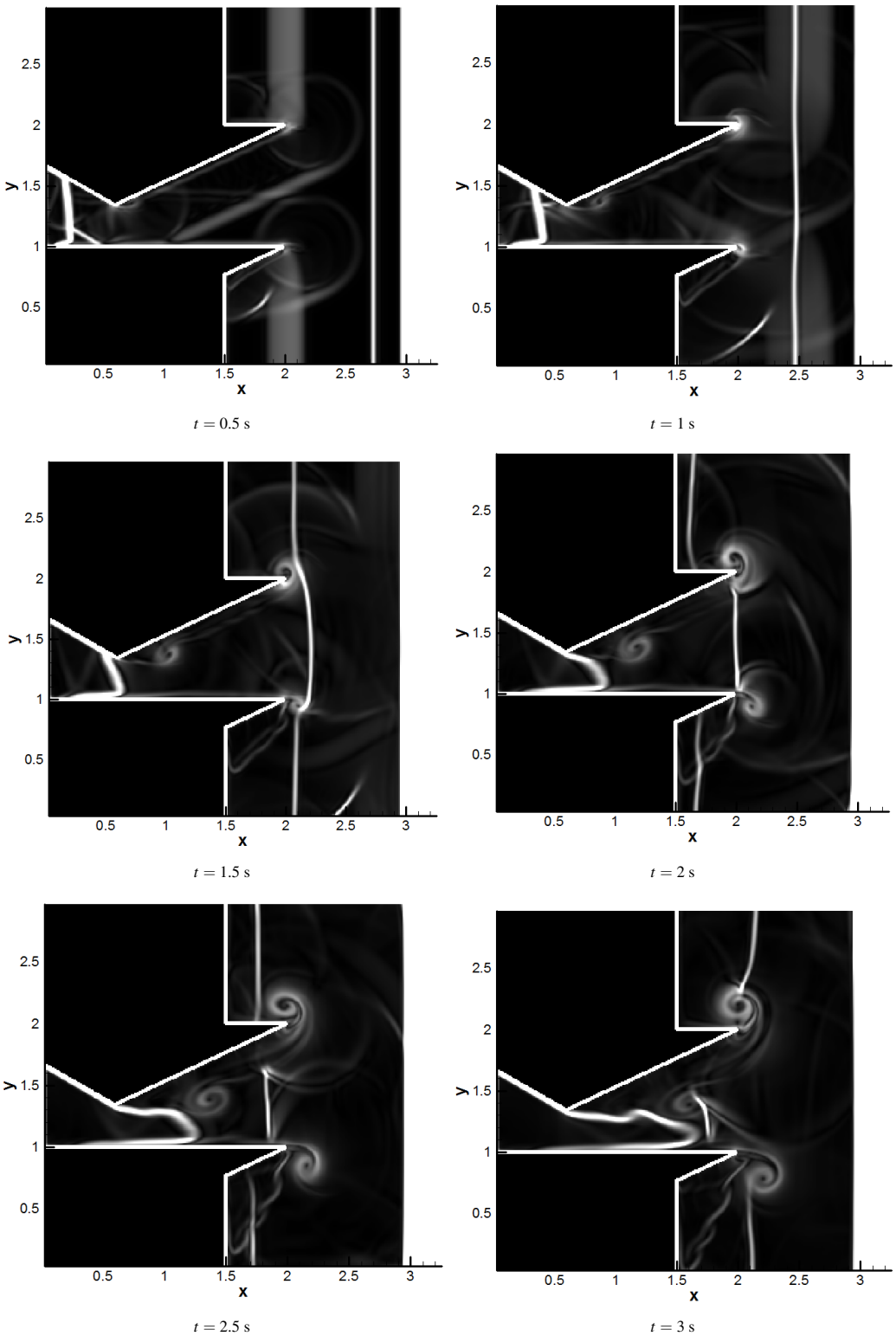

Figure 5. Flow evolution in the nozzle for M = 0.5 and WNND scheme.

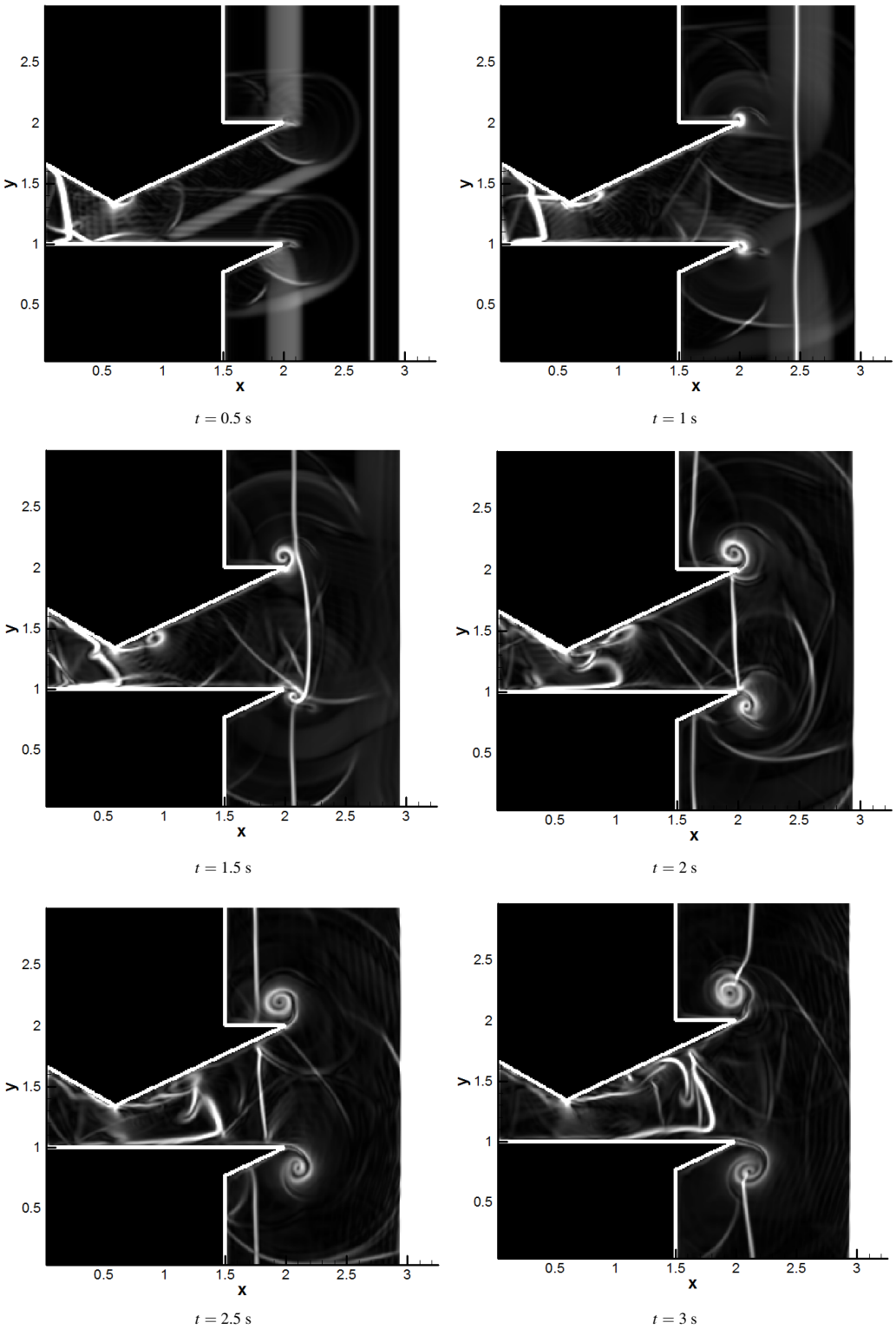

Figure 6. Flow evolution in the nozzle for M = 0.5 and WENO scheme.

of the flow inside the nozzle for a case with an inlet Mach number of 0.8. Here, it is also evident that at 0.5 seconds, initial flow instabilities begin to appear, with small vortex structures forming near shocks and the boundary layer inside the nozzle. This situation indicates that intense interaction between the shock and the boundary layer leads to the development of complex instabilities and density fluctuations. At 1.5 and 2 seconds, larger and more complex vortex structures emerge along the flow path, a direct result of repeated shockwave and boundary-layer interactions. These interactions induce strong dynamic responses in the density gradients, causing larger instabilities in different parts of the flow. By 2.5 seconds, these unstable structures have developed significantly, with shock waves appearing in intricate, intertwined shapes, reflecting intense interactions between shocks and the boundary layer under high-speed

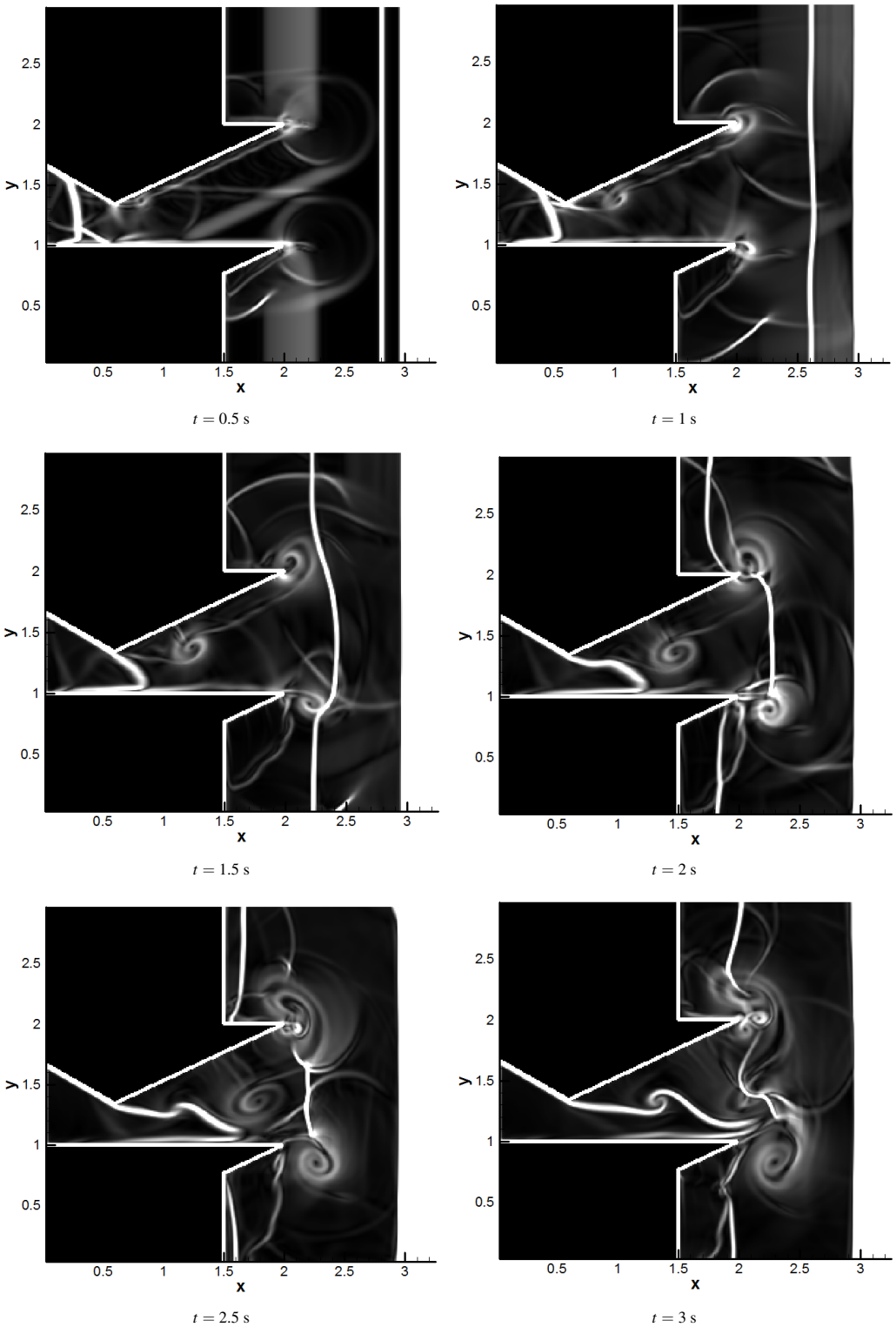

Figure 7. Flow evolution in the nozzle for M = 0.8 and WNND scheme.

and unsteady flow conditions.

Figures 9 and 10 show distributions of density and Mach number for both laminar and turbulent flows. Results of WNND and WENO discretization schemes are presented for comparison purposes. It is worth mentioning that the entrance Mach number is 0.5.

In the laminar flow, density contours and Mach number are observed to be relatively organized and stable, indicating that the flow is in a relatively equilibrium and calm state. The interactions between shock waves and the boundary layer are minimal, and there are no significant dynamic instabilities. This condition mainly reflects a stable flow state where shocks and boundary layers have gentle, low-energy interactions, and modeling this situation is close to reality. However, in turbulent flow, more unstable and complex structures are observed, indicating stronger interactions be-

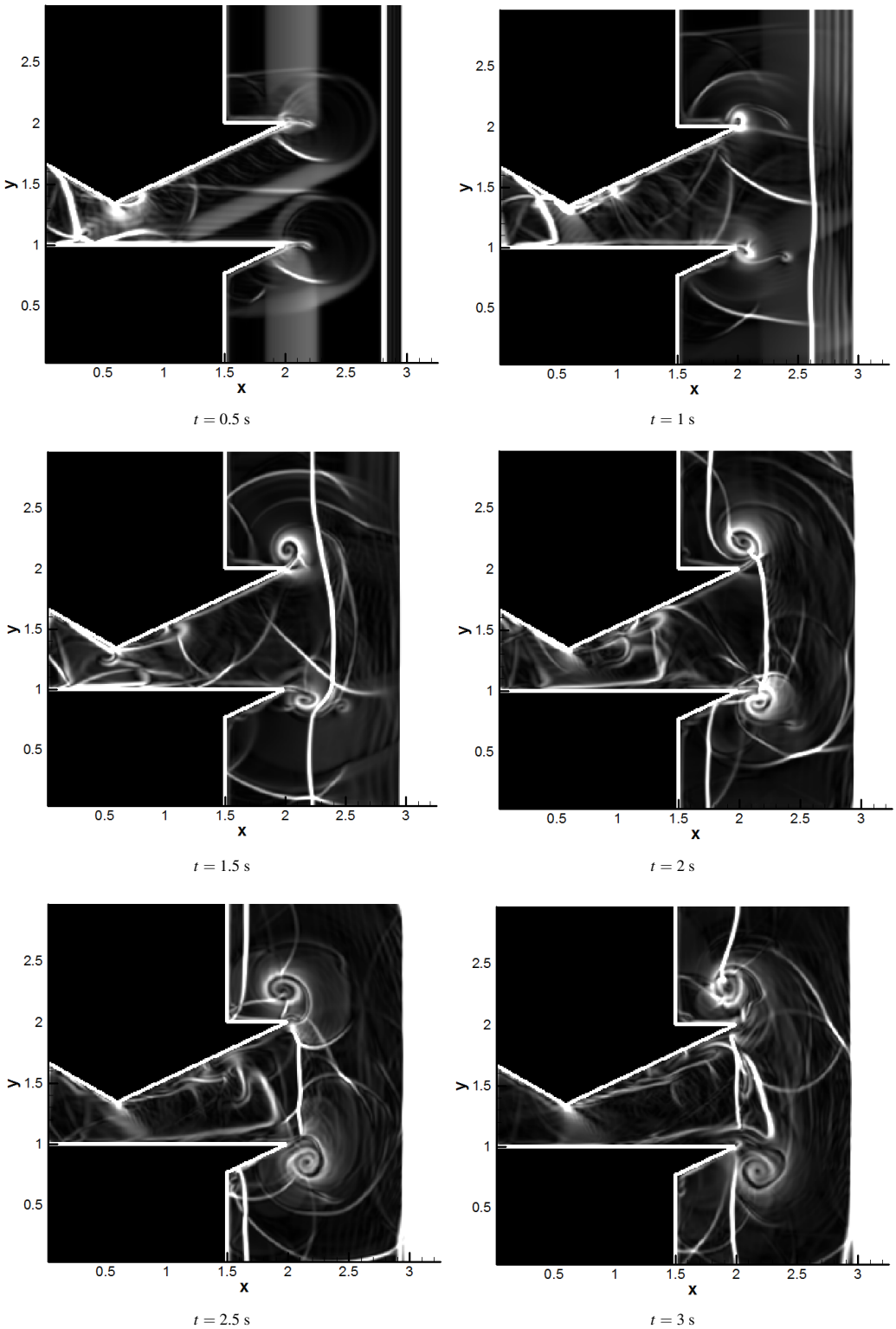

Figure 8. Flow evolution in the nozzle for M = 0.8 and WENO scheme.

tween shock waves, the boundary layer, and dynamic instabilities. In this state, the shock waves interacting with the boundary layer, reflected waves, and continuous interference lead to the formation of intricate and unstable patterns. Modeling such turbulent flows is challenging and requires turbulence and instability models that are not yet sufficiently close to physical reality. Nevertheless, high-order discretization methods like WENO and turbulent flow models have been somewhat successful in simulating flow structures with acceptable accuracy.

Modeling turbulent flows is very complex because of dynamic instabilities, wave interactions, and the formation of intricate structures at multiple scales hinder close approximation to actual conditions. Numerical discretization

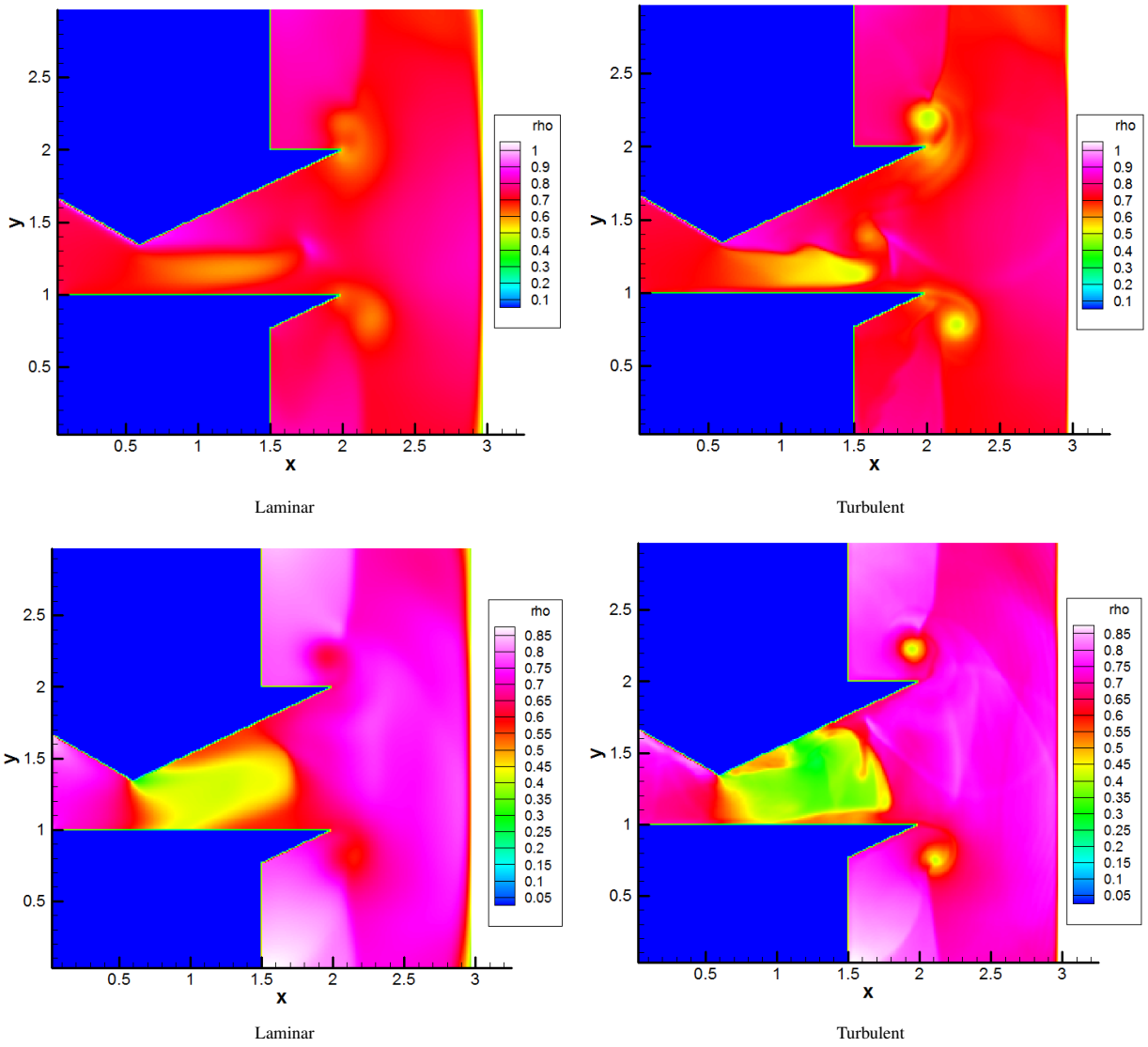

Figure 9. Comparison of density distribution for laminar and turbulent flows at $t = 3$ s (upper row: WNND, lower row: WENO).

techniques such as WNND and WENO have been able to simulate unstable structures with acceptable accuracy but still fall short of representing all details and physical realities fully. Turbulent models cannot reproduce every detail completely; however, with appropriate adjustments and parameters, it is possible to achieve reliable results for engineering analyses.

In the following, density distribution on the bottom wall and horizontal velocity on line $y = 1.25$ are presented for both laminar and turbulent flows. Figures 11 and 12 are for WNND and figures 13 and 14 are for WENO scheme.

In these comparison charts, both the laminar and turbulent models similarly predict the increasing and decreasing trends of density and horizontal velocity. However, notable differences in the results of modeling laminar and turbulent flows inside the nozzle are observed in certain regions when using the WNND and WENO methods. Specifically, for the density distribution in laminar and turbulent flows, discrepancies are seen near the throat with the WNND method, but regarding the horizontal velocity distribution around $x = 1.5$, the difference between laminar and turbulent models is more pronounced. In the remaining points, there is good agreement between the results of laminar and turbulent flow models.

In the WENO method, the differences between laminar and turbulent model results for density and horizontal velocity near $x = 1.5$ are noticeable, while at other points, the results show relatively good agreement. Therefore, it can be concluded that the WNND method performs weaker because it does not similarly predict the flow differences in the density and velocity charts. Conversely, the WENO method correctly captures these differences around $x = 1.5$, and where discrepancies exist, the maximal and minimal regions are similar, although their values differ. Essentially, the WENO approach has been able to depict more complex, unstable, and accurate flow structures in the velocity distribution, whereas the WNND method has less capability in predicting finer details.

The effects of discretization schemes are studied for two entrance Mach numbers (0.5 and 0.8) and depicted in figures 15 and 16.

Based on figures 15 and 16, both discretization methods

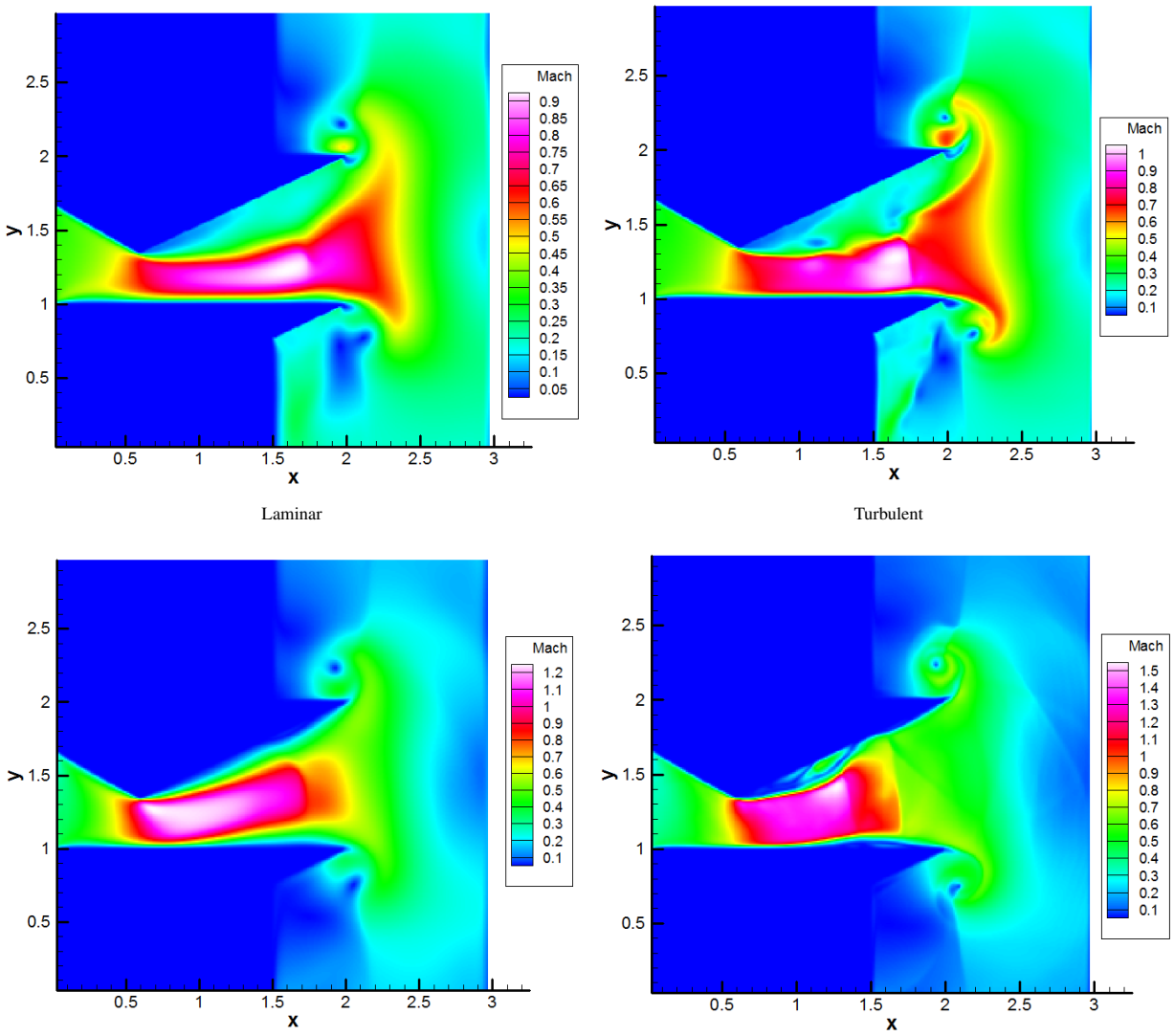

Figure 10. Comparison of Mach number distribution for laminar and turbulent flows at $t = 3$ s (upper row: WNND, lower row: WENO).

are capable of reconstructing the overall density and horizontal velocity structures, including rising and falling regions along the wall. Under specific conditions such as low-amplitude, steady flows, they can operate similarly and produce acceptable results. However, the WENO method, due to its superior ability to model complex phenomena, small-scale structures, and dynamic instabilities, exhibits more fluctuations and intricate features in the density and velocity distributions. Conversely, the WNND method produces simpler, smoother results, indicating its limitations in capturing unstable details and small structures within the flow.

These differences are also evident in figures 17 and 18. Notably, the WNND method does not accurately predict the increase in flow speed after the throat, and the density distribution remains nearly constant across a significant portion of the nozzle length. Overall, the WENO method, thanks to its high capability to simulate small-scale and unstable dynamic structures, provides results that are closer to the physical realities in complex scenarios. Meanwhile, the WNND approach, while effective in low-amplitude, steady flows due to its simplicity, diverges from actual flow behavior in unsteady, dynamic conditions.

Ultimately, the effects of the inlet Mach number on the density distribution along the wall and the horizontal velocity distribution along the line has been examined, with the results presented in figures 19 and 20 for the WNND method, and in figures 21 and 22 for the WENO method.

It is expected that as the inlet Mach number increases, the flow velocity will also increase up to just before the flow reaches the shock, resulting in higher velocity values. However, the WNND method fails to reliably capture this behavior and is not trustworthy in this regard. Overall, the wall density decreases as the Mach number rises, a trend that is evident in both methods.

Based on figures above, when the inlet Mach number increases, the horizontal velocity shows a significant rise, which suddenly drops with the formation of a shock wave. This behavior is well predicted by the WENO method, but the WNND method fails to capture this trend accurately and even underestimates the abrupt density increase caused by the shock.

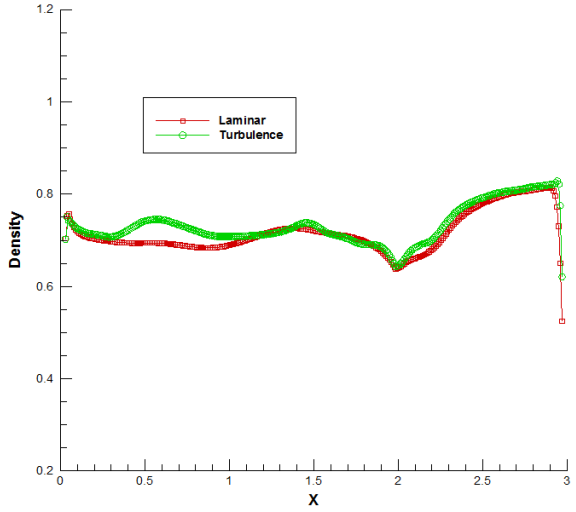

Figure 11. Density distribution on the nozzle bottom wall for laminar and turbulent flows at $t = 3$ s, WNND scheme.

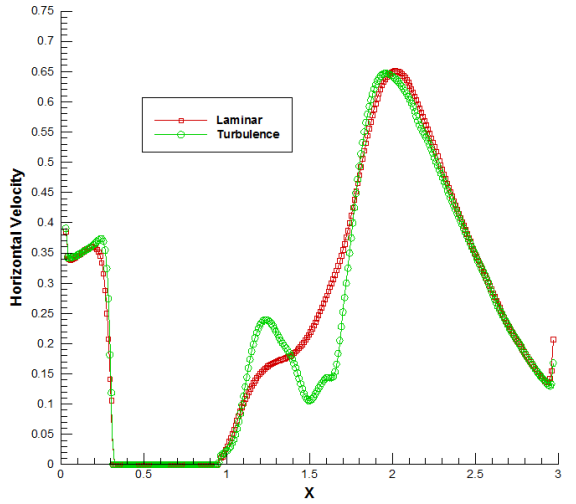

Figure 12. Horizontal velocity distribution on line $y = 1.25$ for laminar and turbulent flows at $t = 3$ s, WNND scheme.

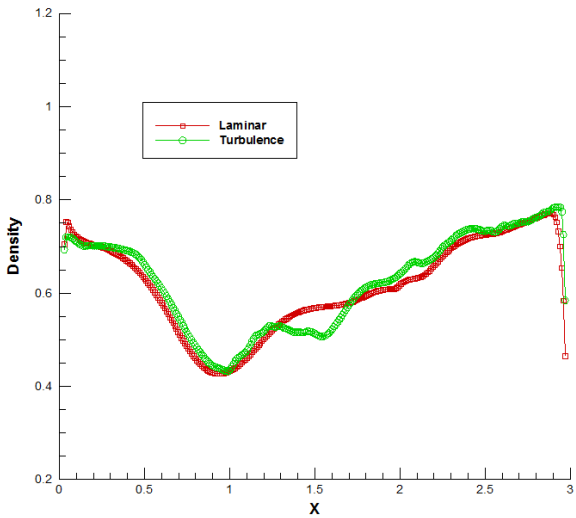

Figure 13. Density distribution on the nozzle bottom wall for laminar and turbulent flows at $t = 3$ s, WENO scheme.

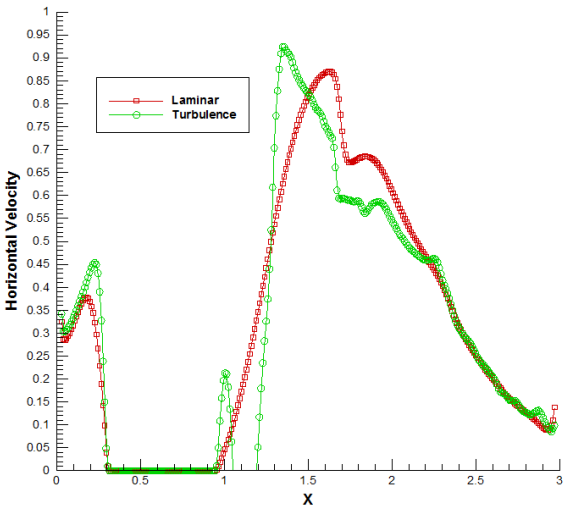

Figure 14. Horizontal velocity distribution on line $y = 1.25$ for laminar and turbulent flows at $t = 3$ s, WENO scheme.

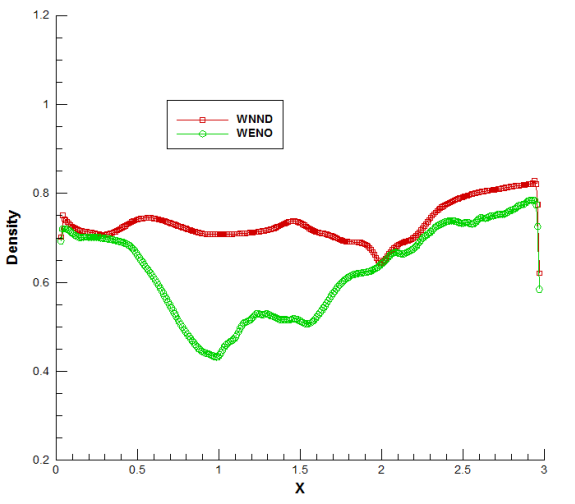

Figure 15. Comparison of WNND and WENO discretization schemes on bottom wall density distribution for M = 0.5.

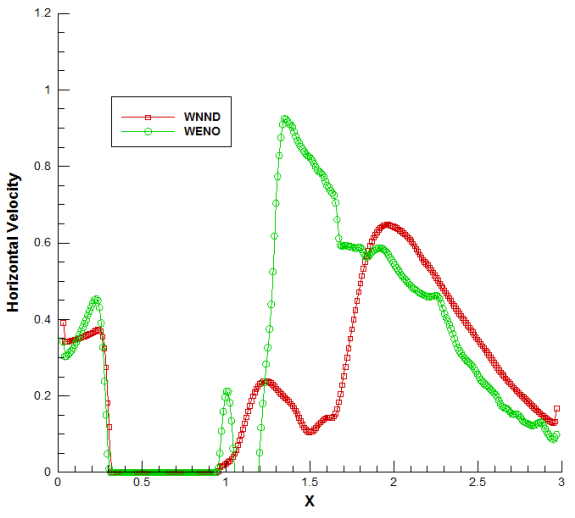

Figure 16. Comparison of WNND and WENO discretization schemes on line $y = 1.25$ horizontal velocity distribution for M = 0.5.

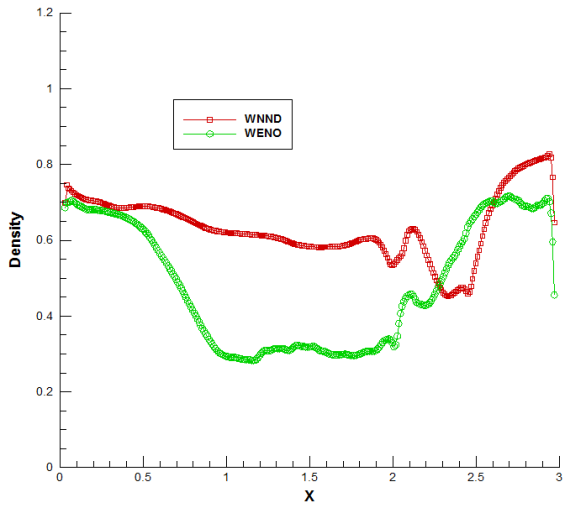

Figure 17. Comparison of WNND and WENO discretization schemes on bottom wall density distribution for M = 0.8.

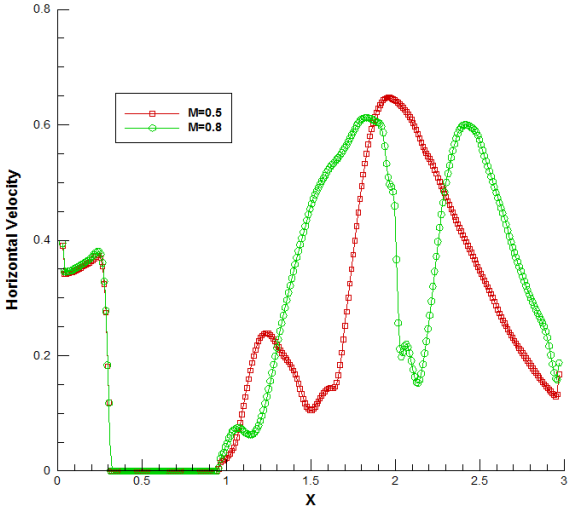

Figure 20. Effects of Mach number on horizontal velocity distribution for WNND scheme.

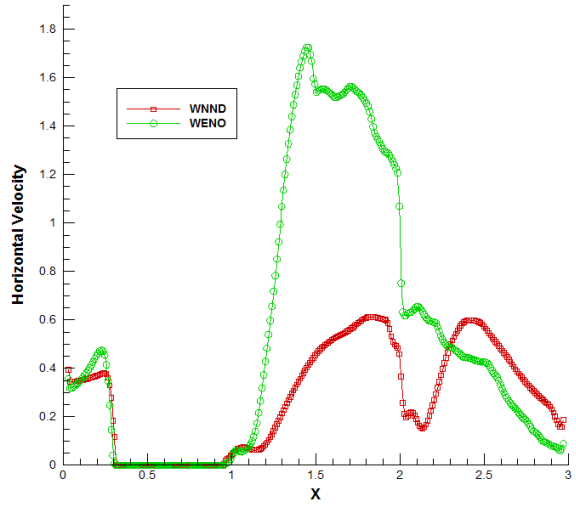

Figure 18. Comparison of WNND and WENO discretization schemes on line $y = 1.25$ horizontal velocity distribution for M = 0.8.

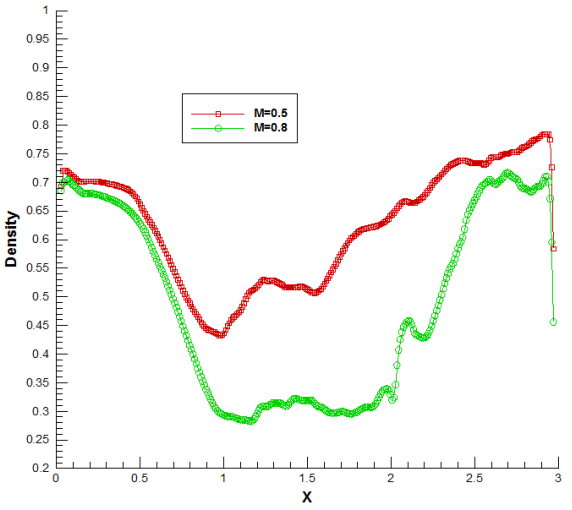

Figure 21. Effects of Mach number on density distribution for WENO scheme.

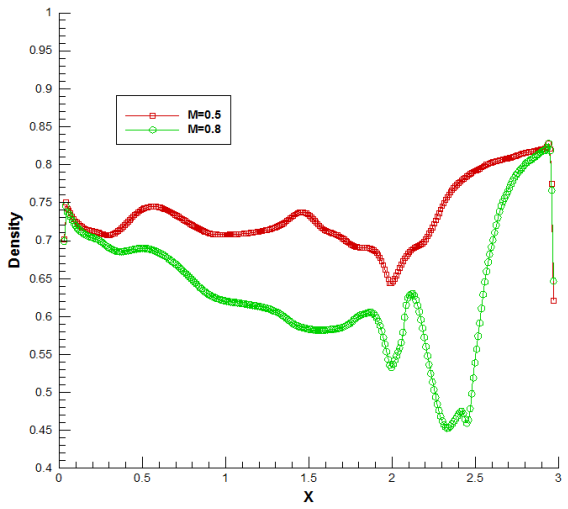

Figure 19. Effects of Mach number on density distribution for WNND scheme.

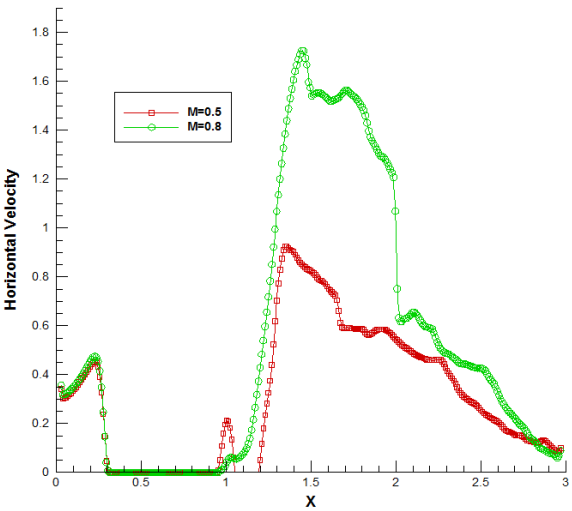

Figure 22. Effects of Mach number on horizontal velocity distribution for WNND scheme.

4. Conclusion

In this study, two different spatial discretization schemes are employed to evaluate the effectiveness of a double distribution function lattice Boltzmann method (LBM) for analyzing shock wave-boundary layer interaction in a nozzle. Specifically, the fifth-order WENO (Weighted Essentially Non-Oscillatory) scheme and the third-order WNND (Weighted Non-Negativity-Preserving Discretization) scheme are compared based on density and velocity distribution. Temporal discretization is accomplished via the third-order Runge-Kutta method.

The overall conclusion is that in regions where the results of both methods are close, the flow is in a steady state without significant instabilities. The interaction between the shock and boundary layer is weak, meaning the shock wave is strong or dynamic complexities are inactive in these zones. In such cases, static and steady structures dominate, and the flow modeling in these regions is relatively simple and linear—indicating laminar flow conditions without signs of turbulence or instability.

However, looking at the horizontal velocity plots, there are areas where the differences between the two discretization methods are highly significant, indicating that the WENO method can reveal more complex structures, instabilities, and higher fluctuations in the shock-boundary layer interaction. Conversely, the WNND method shows smoother, less detailed behavior, suggesting it cannot accurately reproduce the unstable phenomena and active interactions occurring in the interaction zone. The notable disparities in some regions highlight the presence of strong dynamic interactions, reflective waves, and active instabilities, signifying the existence of small-scale structures and considerable dynamic complexity within the flow.

In regions where significant differences are observed between the results of the two discretization methods, WNND and WENO, it can be concluded that the shock-boundary layer interaction is active and unstable in those areas. Shock waves, reflections, and dynamic instabilities lead to the formation of small-scale structures and intense fluctuations within the flow. Conversely, in zones where the results of both methods are nearly aligned, the interaction is in a low-amplitude or steady state, with the overall flow structures remaining relatively stable and predictable.

Overall, the density distribution along the wall and the horizontal velocity profiles along constant y-lines indicate that active and complex interactions occur between shock waves and the boundary layer in parts of the flow, where dynamic instabilities, wave reflections, and small-scale structures play significant roles. High-order and detail-sensitive discretization approaches like WENO are better at capturing these active interactions, providing results closer to the actual flow dynamics. In stable regions, simpler interactions and relatively fixed structures dominate, and both methods produce similar results.

Authors Contribution
The intellectual substance, idea, and design of this study, or the analysis and interpretation of the data (if applicable), as well as the manuscript's writing, were all sufficiently contributed to by each author.

Availability of data and materials
The data that support the findings of this study are available from the corresponding author upon reasonable request.

Conflict of interests
The authors declare that they have no known competing financial interests or personal relationships that could have appeared to influence the work reported in this paper.

References

[1] D. S. Dolling. "Fifty years of shock-wave/boundary-layer interaction research: What next?". *AIAA Journal*, **39**(8), 2001.

[2] Q. Kun. "Development of lattice Boltzmann method for compressible flows.". PhD dissertation, National University of Singapore, 2008.

[3] A. G. Xu, G. C. Zhang, Y. B. Gan, F. Chen, and X. J. Yu. "Lattice Boltzmann modeling and simulation of compressible flows.". *Front. Phys*, **7**(7):582–600, 2012.

[4] K. Li and C. Zhong. "A lattice Boltzmann model for simulation of compressible flows.". *International Journal for Numerical Methods in Fluids*, 2014.

[5] Q. Li, Y. L. He, Y. Wang, and W. Q. Tao. "Coupled double-distribution-function lattice Boltzmann method for the compressible Navier-Stokes equations.". *Physical review E*, **76**, 2007.

[6] R. F. Qiu, Y. C. You, C. X. Zhu, and R. Q. Chen. "Lattice Boltzmann simulation for high-speed compressible viscous flows with a boundary layer.". *Applied Mathematical Modeling*, 48:567–583, 2017.

[7] A. Jammalamadaka, Y. Li, P. Gopalakrishnan, R. Zhang, and H. Chen. "Simulation of a canonical shock wave-boundary layer interaction using an LBM-VLES approach.". *Aviation Forum, Fluid Dynamics Conference, Atlanta, Georgia*, 2018.

[8] R. F. Qiu, H. H. Che, T. Zhou, J. F. Zhu, and Y. C. You. "Lattice Boltzmann simulation for unsteady shock wave/boundary layer interaction in a shock tube.". *Computers and Mathematics with Applications*, 2020.

[9] A. Bhadauria, B. Dorschner, and I. Karlin. "Lattice Boltzmann method for fluid-structure interaction in compressible flow.". *Physics of Fluids*, **33**, 2021.

[10] H. Hosseini and E. Goshtasbirad. "Assessment of a compressible lattice Boltzmann method in analyzing shaock wave/boundary layer interaction in a supersonic inlet.". *Journal of Theoretical and Applied Physics*, **18**(6):1–12, 2024.

[11] S. M. Mousavi, R. Pourabidi, and E. Goshtasbi-Rad. "Numerical investigation of over expanded flow behavior in a single expansion ramp nozzle.". *Acta Astronautica*, **146**:273–281, 2018.

Appendix A

Double distribution function methods are evolved upon the fact that energy needs a separate distribution function to be coupled with the density distribution function via the equation of state and acts as a serious alternative for conventional CFD methods in solving Navier-Stokes equations. Accordingly, there will be another equilibrium distribution function for energy. The method by Li et al. [5] is introduced as follows:

The following equations should be solved for density and energy distribution functions:

$$\frac{\partial f_i}{\partial t}+\mathbf{e}_i\cdot\nabla f_i=-\frac{1}{\tau_f}(f_i-f_i^{eq}) \tag{A 1}$$

$$\frac{\partial h_i}{\partial t}+\mathbf{e}_i\cdot\nabla h_i=-\frac{1}{\tau_h}(h_i-h_i^{eq})+\frac{\mathbf{e}_i\cdot u}{\tau_{hf}}(f_i-f_i^{eq}) \tag{A 2}$$

where f_i and h_i are density and energy distribution functions, respectively with their corresponding equilibrium distribution functions f_i^{eq} and h_i^{eq}. $\mathbf{e}_i$ is discrete velocity and τ_f and τ_h are relaxation times for density and energy, respectively. In which $\tau_{hf}=\tau_h\tau_f/(\tau_f-\tau_h)$.

The velocity set is defined as:

$$\frac{\mathbf{e}_i}{\sqrt{RT_c}}=\begin{cases}(0,0) & i=0\\ \text{cyc}:(\pm1,0) & i=1,2,3,4\\ \text{cyc}:\sqrt{2}(\pm1,\pm1) & i=5,6,7,8\\ \text{cyc}:2(\pm1,0) & i=9,10,11,12\end{cases} \tag{A 3}$$

By use of the Chapman-Enskog expansion, Navier-Stokes equations are derived as:

$$\frac{\partial\rho}{\partial t}+\frac{\partial\rho u_\alpha}{\partial x_\alpha}=0 \tag{A 4}$$

$$\frac{\partial\rho u_\alpha}{\partial t}+\frac{\partial\rho u_\alpha u_\beta}{\partial x_\beta}+\frac{\partial\rho}{\partial x_\alpha}=\frac{\partial\acute{P}_{\alpha\beta}}{\partial x_{\alpha\beta}} \tag{A 5}$$

$$\frac{\partial\rho E}{\partial t}+\frac{\partial(\rho E+\rho)u_\alpha}{\partial x_\alpha}=\frac{\partial}{\partial x_\beta}(\lambda\frac{\partial T}{\partial x_\beta}+\acute{P}_{\alpha\beta}u_\alpha) \tag{A 6}$$

where $p=\rho RT$ and

$$\acute{P}_{\alpha\beta}=\mu\left(\frac{\partial u_\alpha}{\partial x_\beta}+\frac{\partial u_\beta}{\partial x_\alpha}-\frac{2}{D}\frac{\partial u_\chi}{\partial x_\chi}\delta_{\alpha\beta}\right)+\mu_B\frac{\partial u_\chi}{\partial x_\chi}\delta_{\alpha\beta}.$$

Parameters in equation (A 6) are defined as follows:

$$\mu=\tau_f\rho,\ \ \mu_B=\left(\frac{2}{D}+\frac{2}{b}\right)\tau_p f,\ \ \lambda=\tau_h c_p p \tag{A 7}$$

Macroscopic variables are obtained by the following relations:

$$\rho=\sum_i f_i,\ \ u=\sum_i f_i\frac{\mathbf{e}_i}{\rho},\ \ T=2\frac{\sum_i h_i/\rho-|u|^2/2}{bR} \tag{A 8}$$

More details regarding the equilibrium distribution functions as well as the second-order Implicit Explicit (IMEX) Runge-Kutta method are outlined in [5]. Two different schemes are considered for spatial discretization. The fifth-order WENO scheme with a 7-point stencil and the third-order WNND scheme with a 5-point stencil. In the WENO scheme, the convective term is defined as follows:

$$\frac{\partial e_{\alpha x}f_{\alpha,I,J}}{\partial x}=\frac{1}{\Delta x}(\hat{F}_{\alpha,I+1/2,J}-\hat{F}_{\alpha,I-1/2,J}) \tag{A 9}$$

where $e_{\alpha x}$ is the x component of e_α, $\hat{F}_{\alpha,I+1/2,J}$ is the numerical flux at the interface of $x_I+\Delta x/2$ which is defined as:

$$\hat{F}_{\alpha,I+1/2,J}=w_1\hat{F}^1_{\alpha,I+1/2,J}+w_2\hat{F}^2_{\alpha,I+1/2,J}+w_3\hat{F}^3_{\alpha,I+1/2,J} \tag{A 10}$$

Under condition $e_{\alpha x}\geq 0$, these three fluxes are given by:

$$\hat{F}^1_{0,\alpha,I+1/2,J}=\frac{1}{3}F_{\alpha,I-2,J}-\frac{7}{6}F_{\alpha,I-1,J}+\frac{11}{6}F_{\alpha,I,J} \tag{A 11}$$

$$\hat{F}^2_{0,\alpha,I+1/2,J}=-\frac{1}{6}F_{\alpha,I-1,J}-\frac{5}{6}F_{\alpha,I,J}+\frac{1}{3}F_{\alpha,I+1,J} \tag{A 12}$$

$$\hat{F}^3_{0,\alpha,I+1/2,J}=\frac{1}{3}F_{\alpha,I,J}+\frac{5}{6}F_{\alpha,I+1,J}-\frac{1}{6}F_{\alpha,I+2,J} \tag{A 13}$$

where $F_{\alpha,I,J}=e_{\alpha x}f_{\alpha,I,J}$.

The weighting factors are given by:

$$w_q=\frac{\tilde{w}_q}{\tilde{w}_1+\tilde{w}_2+\tilde{w}_3} \tag{A 14}$$

$$w_q=\frac{\delta_q}{(10^{-6}+\sigma_q)^2} \tag{A 15}$$

with $\delta_1=1/10$, $\delta_2=3/5$, $\delta_3=3/10$. Coefficients σ_{qs} are smoothness indicators defined by:

$$\begin{aligned}\sigma_1=&\frac{13}{12}(F_{\alpha,I-2,J}-2F_{\alpha,I-1,J}+F_{\alpha,I,J})^2+\\ &\frac{1}{4}(F_{\alpha,I-2,J}-4F_{\alpha,I-1,J}+3F_{\alpha,I,J})^2\end{aligned} \tag{A 16}$$

$$\begin{aligned}\sigma_2=&\frac{13}{12}(F_{\alpha,I-1,J}-2F_{\alpha,I,J}+F_{\alpha,I+1,J})^2+\\ &\frac{1}{4}(F_{\alpha,I-1,J}-F_{\alpha,I+1,J})^2\end{aligned} \tag{A 17}$$

$$\begin{aligned}\sigma_3=&\frac{13}{12}(F_{\alpha,I,J}-2F_{\alpha,I+1,J}+F_{\alpha,I+2,J})^2+\\ &\frac{1}{4}(3F_{\alpha,I,J}-4F_{\alpha,I+1,J}+F_{\alpha,I+2,J})^2\end{aligned} \tag{A 18}$$

For the WNND scheme:

$$\frac{\partial e_{\alpha x}f_{\alpha,I,J}}{\partial x}=\frac{1}{\Delta x}(\hat{F}_{\alpha,I+1/2,J}-\hat{F}_{\alpha,I-1/2,J}) \tag{A 19}$$

where $\hat{F}_{\alpha,I+1/2,J}$ is the numerical flux at the interface of $x_I+\Delta x/2$, and given by:

$$\hat{F}_{\alpha,I+1/2,J}=\hat{F}^+_{\alpha,I+1/2,J}+\hat{F}^-_{\alpha,I+1/2,J} \tag{A 20}$$

In which $\hat{F}^+_{\alpha,I+1/2,J}$ and $\hat{F}^-_{\alpha,I+1/2,J}$ are the positive and negative numerical fluxes, respectively. We go through the following just for the positive part since the negative one should be extracted symmetrically.

$$\hat{F}^+_{\alpha,I+1/2,J}=\sum_{k=0}^{1}w_k\hat{F}^+_{k,\alpha,I+1/2,J} \tag{A 21}$$

where:

$$\begin{aligned}\hat{F}^{+}_{0,\alpha,I+1/2,J} &= -\frac{1}{2}\hat{F}^{+}_{\alpha,I-1,J} + \frac{3}{2}\hat{F}^{+}_{\alpha,I,J},\\ \hat{F}^{+}_{1,\alpha,I+1/2,J} &= \frac{1}{2}\hat{F}^{+}_{\alpha,I,J} + \frac{3}{2}\hat{F}^{+}_{\alpha,I+1,J}\end{aligned} \tag{A 22}$$

$\hat{F}^{+}_{\alpha,I,J}$ and $\hat{F}^{-}_{\alpha,I,J}$ are defined as:

$$\hat{F}^{+}_{\alpha,I,J} = \frac{1}{2}(e_{\alpha x} + |e_{\alpha x}|) f_{\alpha,I,J} \tag{A 23}$$

$$\hat{F}^{-}_{\alpha,I,J} = \frac{1}{2}(e_{\alpha x} - |e_{\alpha x}|) f_{\alpha,I,J} \tag{A 24}$$

Weights are calculated as:

$$w_k = \frac{\alpha_k}{\sum_{l=0}^{1}\alpha_l},\ k = 0,1 \tag{A 25}$$

In which coefficients α_k are as follows for the WNND-Z scheme:

$$\alpha_k = d_k(1.0 + \frac{\beta_k}{IS_k + \varepsilon},\ k = 0,1 \tag{A 26}$$

where d_k are the ideal weights with the values $d_0 = 1/3$ and $d_1 = 2/3$, and the value of ε is 10^{-6}. The expression of IS_k and β_k are:

$$IS_0 = (F^{+}_{\alpha,I,J} - F^{+}_{\alpha,I-1,J})^2 \tag{A 27}$$

$$IS_1 = (F^{+}_{\alpha,I+1,J} - F^{+}_{\alpha,I,J})^2 \tag{A 28}$$

$$\begin{aligned}\beta_z &= \left| IS_{GZ} - \frac{IS_0 + IS_1}{2} \right|,\\ IS_{GZ} &= \frac{1}{4}(F^{+}_{\alpha,I+1,J} - F^{+}_{\alpha,I-1,J})^2\end{aligned} \tag{A 29}$$